The Astronomical Journal, 167:32 (12pp), 2024 January https://doi.org/10.3847/1538-3881/ad0e02

Coma Abundances of Volatiles at Small Heliocentric Distances: Compositional Measurements of Long-period Comet C/2020 S3 (Erasmus)

Chemeda Ejeta[1], Erika Gibb[1], Nathan Roth[2,3], Michael A. DiSanti[2], Neil Dello Russo[4], Mohammad Saki[1,5], Adam J. McKay[6], Hideyo Kawakita[7], Younas Khan[8], Boncho P. Bonev[9], Ronald J. Vervack, Jr.[4], and Michael R. Combi[10]

[1] Department of Physics and Astronomy, University of Missouri–St. Louis, Saint Louis, MO 63121, USA
[2] Solar System Exploration Division, Planetary Systems Laboratory, MS 693, NASA Goddard Space Flight Center, Greenbelt, MD 20771, USA
[3] Catholic University of America, Washington, DC 20064, USA
[4] Space Department, Johns Hopkins University Applied Physics Laboratory, Laurel, MD 20723, USA
[5] Auburn University, Auburn, AL 36849, USA
[6] Department of Physics and Astronomy, Appalachian State University, Boone, NC 28608-2106, USA
[7] National Astronomical Observatory of Japan, 2-21-1 Osawa, Mitaka, Tokyo 181-8588, Japan
[8] University of Alabama at Birmingham, Birmingham, AL 35294, USA
[9] Department of Physics, American University, Washington, DC 20016, USA
[10] Department of Climate and Space Sciences and Engineering, University of Michigan, Ann Arbor, MI 48109, USA
Received 2023 August 24; revised 2023 November 11; accepted 2023 November 15; published 2023 December 22

Abstract

We report production rates of H_2O and nine trace molecules (C_2H_6, CH_4, H_2CO, CH_3OH, HCN, NH_3, C_2H_2, OCS, and CO) in long-period comet C/2020 S3 (Erasmus) using the high-resolution, cross-dispersed infrared spectrograph (iSHELL) at the NASA Infrared Telescope Facility, on two pre-perihelion dates at heliocentric distances $R_h = 0.49$ and 0.52 au. Our molecular abundances with respect to simultaneously or contemporaneously measured H_2O indicate that S3 is depleted in CH_3OH compared to its mean abundance relative to H_2O among the overall comet population (Oort Cloud comets and Jupiter-family comets combined), whereas the eight other measured species have near-average abundances relative to H_2O. In addition, compared to comets observed at $R_h < 0.80$ au at near-infrared wavelengths, S3 showed enhancement in the abundances of volatile species H_2CO, NH_3, and C_2H_2, indicating possible additional (distributed) sources in the coma for these volatile species. The spatial profiles of volatile species in S3 in different instrumental settings are dramatically different, which might suggest temporal variability in comet outgassing behavior between the nonsimultaneous measurements. The spatial distributions of simultaneously measured volatile species C_2H_6 and CH_4 are nearly symmetric and closely track each other, while those of CO and HCN co-measured with H_2O (using different instrument settings) are similar to each other and are asymmetric in the antisunward direction.

Unified Astronomy Thesaurus concepts: Comet volatiles (2162); Comets (280); Comae (271); Near infrared astronomy (1093)

1. Introduction

Comets are among the small bodies stored in the outer reaches of our solar system. Having experienced minimal alteration from gravitational self-heating, thermal processing, or radiative processing (e.g., DiSanti et al. 2017), their internal compositions are likely to have changed minimally since the formation of the solar system (∼4.5 Gyr ago). Thus, comets likely retain a compositional record of the protoplanetary disk midplane during planet formation (Bockelée-Morvan et al. 2004; Mumma & Charnley 2011; DiSanti et al. 2017).

Comet C/2020 S3 (Erasmus; hereafter S3) was discovered by Nicolas Erasmus of the Asteroid Terrestrial-Impact Last Alert System on UT 2020 September 17. S3 reached perihelion ($R_h \sim 0.4$ au) on UT 2020 December 12 and was closest to Earth (1.03 au) on 2020 November 19. The reciprocal semimajor axis after integrating the orbit backward to a time before any planetary perturbations, $1/a_0$, is approximately inversely related to the square of the number of inner solar system crossings (A'Hearn et al. 1995). Królikowska & Dybczynski (2017) analyzed the dynamical simulation of long-period comets having perihelia farther than 3.1 au from the Sun. They showed that all dynamically old comets have $1/a_0 > 25 \times 10^{-6}$ au^{-1} ($a_0 < 40{,}000$ au). Thus, with $1/a_0$ of $\sim 5 \times 10^{-3}$ au^{-1} (Nakano Note 4506), S3 is a dynamically old comet that has previously visited the inner solar system.

Comets such as S3 are from the Oort Cloud and therefore have long orbital periods (Vokrouhlicky et al. 2019). As comets approach the inner solar system, increasing insolation causes nucleus ices to sublimate. The released volatiles and refractory material (dust dragged by sublimating gases) lead to the development of an expanding atmosphere (i.e., coma). High-resolution, near-infrared (NIR) spectroscopy is a valuable tool to characterize the composition of volatiles (ices) in comet nuclei through the analysis of fluorescent emissions from H_2O, CO, CH_4, C_2H_6, HCN, NH_3, C_2H_2, H_2CO, OCS, and CH_3OH in the coma. The nucleus composition inferred from these studies can also place observational constraints on the nascent protoplanetary disk midplane where comets formed (Eistrup et al. 2019; Willacy et al. 2022).

Although our understanding of comet composition has evolved in recent years, the sample size of ∼30 Oort Cloud comets (OCCs; dominated by observations at $R_h > 0.8$ au) is insufficient to fully represent their compositional diversity,

Table 1
iSHELL Observing Log for S3

2020 UT Date	Setting[a]	Target	UT Time	R_h (au)	Δ (au)	$d\Delta/dt$ (km s^{-1})	$T_{\rm int}$ (minutes)	Slit PA (deg)
Nov 29	L-custom	S3	19:32–20:10	0.52	1.10	18.50	40	273
	Lp1	S3	20:26–21:05	0.52	1.10	18.70	30	273
	Lp1	BS 5531	21:11–21:17	⋯	⋯	⋯	⋯	⋯
Dec 1	M2	S3	18:11–18:45	0.49	1.12	21.10	40	272
	L-custom	S3	19:04–20:20	0.49	1.12	21.30	55	272
	L-custom	BS 5531	20:52–20:58	⋯	⋯	⋯	⋯	⋯
	M2	BS 5531	21:18–21:24	⋯	⋯	⋯	⋯	⋯
	Lp1	BS 5531	21:31–21:37	⋯	⋯	⋯	⋯	⋯
	Lp1	S3	21:40–22:10	0.49	1.12	21.70	40	272

Notes. R_h, Δ, and $d\Delta/dt$ are the heliocentric distance, geocentric distance, and geocentric velocity of S3 at the time of observation, respectively, and $T_{\rm int}$ is the total on-source integration time. The slit PA was oriented along the projected Sun–comet line on both dates.
[a] Spectral setting used to sample molecular lines.

making their classification difficult (Crovisier et al. 2004; Dello Russo et al. 2016a). Due to solar avoidance constraints for daytime observations, OCCs measured at $R_h \leqslant 0.80$ au are particularly limited in number. Thus, our observations of S3 at $R_h \sim 0.50$ au are crucial not only to further the development of a taxonomy for comets based on primary volatile composition but also to investigate possible effects of heliocentric distance on composition measurements.

We present production rates and abundance (i.e., mixing ratios) with respect to H_2O and C_2H_6, measuring 11 molecules having fluorescent emissions between ∼2.8 and 5.0 μm: H_2O, C_2H_6, H_2CO, CH_3OH, CH_4, CO, NH_3, HCN, C_2H_2, NH_2, and OCS. In Section 2, we discuss our observations. In Section 3, we discuss our data reduction and analysis. In Section 4, we present our results. Section 5 discusses our results and places them in the context of comets characterized to date.

2. Observations

We observed S3 during the daytime on UT 2020 November 29 and UT December 1 with Director's Discretionary Time, using the high-resolution NIR echelle spectrograph iSHELL (Rayner et al. 2022) at the 3 m NASA Infrared Telescope Facility (IRTF) located at Maunakea, HI. iSHELL is a cross-dispersed infrared spectrometer operating at wavelengths of ∼1–5 μm. For the comet observations, we used a slit 0.″75 (6 pixels) wide and 15″ long. On both dates, we utilized the Lp1 setting, which covers ∼3.28–3.66 μm, to sample C_2H_6, CH_4, H_2CO, CH_3OH, and NH_2 (plus prompt OH, used as a proxy for the production and spatial distribution of its parent, H_2O; Bonev 2005; Bonev & Mumma 2006), as well as a custom *L*-band setting covering ∼2.80–3.10 μm and sampling HCN, C_2H_2, NH_3, and NH_2 together with H_2O. On December 1, we also used the M2 setting, which covers ∼4.52–5.25 μm, to sample CO, OCS, and CN together with H_2O. CO and CH_4 have strong corresponding terrestrial absorptions; therefore, sufficient geocentric Doppler velocity ($|d\Delta/dt| \sim\geqslant 12$ km s^{-1}) is required to shift the cometary emission lines away from the (opaque) cores into the wings of their telluric counterparts (Dello Russo et al. 2016a). The magnitude of the geocentric Doppler shift of S3 on the dates of our observations (∼+18–21 km s^{-1}; see Table 1) was sufficient to measure both CO and CH_4.

Spectra were obtained using a standard ABBA nod pattern to facilitate sky subtraction, with A and B beams in the (15″-long) slit symmetrically displaced about its center and separated by half its length. Combining spectra as A-B-B+A canceled emissions from the thermal background, instrumental biases, and sky emission (lines and continuum) to second order in air mass. The slit was oriented along the projected Sun–comet direction with a position angle (PA) of ∼270° on both dates, to compare the release of material into sunward- versus antisunward-facing hemispheres of the comet with a solar phase angle of ∼60°. To calibrate fluxes, spectra of the bright infrared flux standard star BS 5531 were obtained, using a 4″-wide slit to minimize slit losses. Our observing log is shown in Table 1.

On UT 2020 November 29, the standard-star spectra acquired using the L-custom setting were not usable for flux calibration, due to bad weather conditions. As a result, for this date we computed flux calibration factors (Γ, W m^{-2} cm^{-1} (counts s^{-1})$^{-1}$) from the ratios of their values measured using the Lp1 setting on both nights and the L-custom setting on UT 2020 December 1 (for which photometric conditions persisted throughout the observing period). The atmospheric seeing was also relatively poor (∼1.″5) on November 29 compared to December 1 (∼0.″5–1.″0).

3. Data Reduction and Analysis

We followed data reduction procedures that have been rigorously tested and are described extensively in refereed literature (e.g., Dello Russo et al. 1998; Bonev 2005; DiSanti et al. 2006, 2014; Radeva et al. 2010), including their application to unique aspects of iSHELL spectra (DiSanti et al. 2017). Echelle orders were straightened spatially and spectrally so that each row corresponded to a unique position along the slit and each column to a unique wavelength. Spectra were extracted from the processed orders by summing over 15 rows (approximately 2.″5), seven rows to each side of the nucleus, defined as the peak of continuum emission in each spectral order. Individual A-B pairs were spatially registered to correct for potential comet drift during an exposure sequence; however, we note that these corrections were minimal, due to active IR guiding via narrowband filter imaging near 3.46 μm.

We determined contributions from continuum and gaseous emissions as previously described (e.g., DiSanti et al. 2017) and as illustrated in Figure 1. Column burdens of telluric absorbers were retrieved and quantified using the NASA Planetary Spectrum Generator (Villanueva et al. 2018). The fully resolved transmittance function was convolved to the resolving power of the data (∼4.2×10^4) and scaled to the comet continuum level. Next, to isolate cometary emission lines, we subtracted the modeled continuum. After correcting each modeled *g*-factor (line intensity) for the monochromatic atmospheric transmittance at its Doppler-shifted wavelength

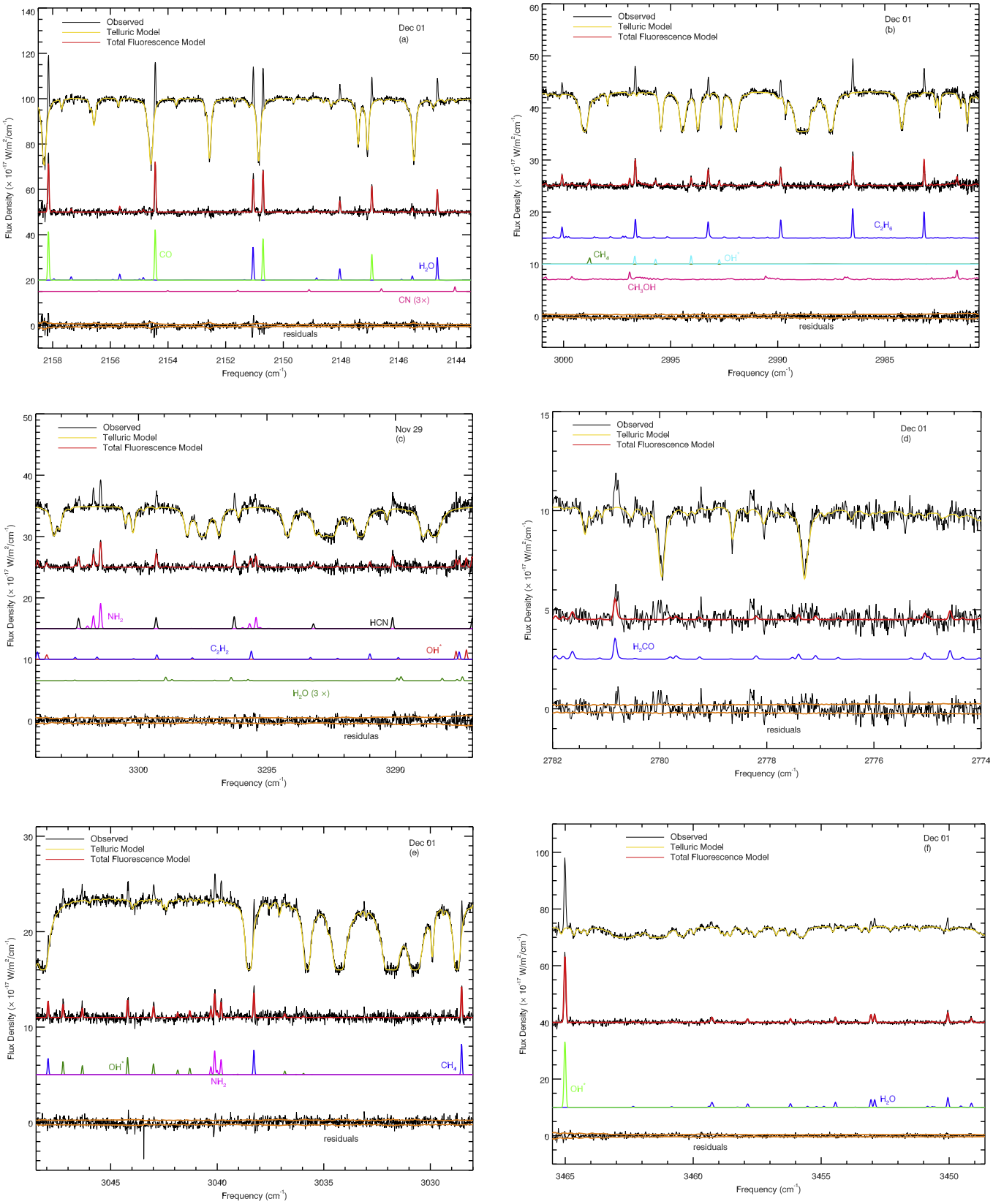

Figure 1. Sample spectra and best-fit fluorescent models of molecular emissions in Erasmus during the observations on 2020 December 1 and November 29. The observed spectra (black) are superimposed with the telluric model (yellow). The total fluorescence model overplotted on the telluric subtracted spectra is shown in red. Individual fluorescence emission models (color-coded by species) are shown below the observed spectrum in each panel. The bottom trace indicates the residual spectrum (after subtracting modeled continuum and total molecular contributions), with the superimposed $\pm 1\sigma$ stochastic noise envelope shown in orange.

(based on the geocentric velocity of the comet at the time of observation), synthetic models of fluorescent emission for each targeted species were compared to observed line intensities. The g-factors used in this study were generated with quantum-mechanical models developed for H_2O (Villanueva et al. 2012b), OH^* (Bonev & Mumma 2006), HCN (Villanueva et al. 2013), NH_3 (Villanueva et al. 2013), NH_2 (Kawakita & Mumma 2011), C_2H_2 (Villanueva et al. 2011b, see Appendix C), C_2H_6 (Villanueva et al. 2011b), CH_3OH (Villanueva et al. 2012a; DiSanti et al. 2013), H_2CO (DiSanti et al. 2006), CH_4 (Gibb et al. 2003), and CO (DiSanti et al. 2001).

4. Results

We determined rotational temperatures ($T_{\rm rot}$), volatile production rates (Q, molecules s^{-1}), and abundances (or "mixing" ratios), e.g., Q_X/Q_{H_2O} or $Q_X/Q_{C_2H_6}$, and spatial profiles for volatile species in S3. The details of this analysis are discussed below.

4.1. Determination of Rotational Temperature

The relative strengths of molecular emission lines are constrained by the excitation conditions in the coma (e.g., Bockelée-Morvan et al. 2004; DiSanti et al. 2016). The strengths of these lines are quantified by a rotational temperature ($T_{\rm rot}$), which needs to be known (either measured or assumed) to determine accurate molecular production rates for each species. When strong lines of a given molecule spanning a broad range of excitation energies can be measured, $T_{\rm rot}$ is obtained using zero-slope excitation analysis (e.g., Dello Russo et al. 2004; Bonev 2005; DiSanti et al. 2006). This technique retrieves the rotational temperature corresponding to a zero slope in $F_{\rm line}/g$ versus $E_{\rm up}$ (or $E_{\rm low}$), where $F_{\rm line}$ is the observed line flux, g is the temperature-dependent fluorescent g-factor, and $E_{\rm up}$ is the upper-state (lower-state) rotational energy of each measured transition (emission line). In S3, H_2O, C_2H_6, HCN, CH_3OH, CO, and H_2CO provided a sufficient number of lines having high signal-to-noise ratio (S/N) and spanning a wide range of rotational energy to obtain a well-constrained $T_{\rm rot}$. As indicated in Table 2, the rotational temperatures determined from these species on both dates are consistent within their 1σ uncertainties. For CH_4, C_2H_2, NH_3, and OCS, accurate rotational temperatures could not be determined, so we assumed the value for H_2O from the same date. This assumption is reasonable, given the consistency among rotational temperatures determined from different species (see Table 2; assumed $T_{\rm rot}$ values are given in parentheses).

4.2. Molecular Production Rates

Nucleus-centered molecular production rates, $Q_{\rm nc}$, are obtained from the line fluxes measured from an extract of 15 spatial rows (as defined in Section 3). In our analysis, emission lines are selected if they are not strongly blended with other species and are in regions of adequate atmospheric transmittance. For a given emission line, $Q_{\rm nc}$ is obtained by applying a coma model that assumes a spherically symmetric gas outflow with uniform velocity and direct nucleus release (e.g., DiSanti et al. 2014, 2016):

$$Q_{\rm nc} = \frac{4\pi\Delta^2 F_{\rm line}}{f(x)\tau_1 g_1},$$

where τ_1(s) is the molecular photodissociation lifetime at $R_h = 1$ au, g_1(W molecule^{-1}) is the fluorescence g-factor at $R_h = 1$ au, Δ (m) is the geocentric distance, and $F_{\rm line}$ (W m^{-2}) is the line flux at the top of the terrestrial atmosphere. The photodissociation timescales of each molecular species and the fluorescence g-factors (given at $R_h = 1$ au) are scaled to the heliocentric distance of our observations using the heliocentric dependence of each quantity (i.e., $\tau = \tau_1 R_h^2$, $g = g_1 R_h^{-2}$, where the subscript "1" refers to values at $R_h = 1$ au). The quantity $f(x)$ is the fraction of the total number of molecules in the coma encompassed by the beam, assuming that their release is entirely from the nucleus, and includes the R_h-dependent molecular scale length, l, given as $l = V_{\rm gas}$ ($R_h = 1$ au) $\tau_1 R_h^{1.5}$ (e.g., DiSanti et al. 2016). The molecular lifetimes used in our analyses are determined using the molecular photodissociation rates in the solar radiation field at $R_h = 1$ au as provided by Huebner & Mukherjee (2015). The gas outflow velocity from the nucleus, $v_{\rm gas} = 800 \times R_h^{-0.5}$ m s^{-1}, is assumed based on velocity-resolved observations of bright comets at radio wavelengths (e.g., Biver et al. 2006). This quantity is not measured directly from our observations since the spectral resolving power of our observation ($\sim 4.2 \times 10^4$) corresponds to a velocity resolution of ~ 7 km s^{-1} and is thus insufficient to resolve spectral lines and hence gas outflow velocities. This assumption of the canonical value of $v_{\rm gas}$ introduces a systematic uncertainty in the production rates; however, this has a negligible effect on our derived abundance ratios (Dello Russo et al. 2020).

Compared to the coma model, slit losses due to atmospheric seeing lower the fraction of molecules within nucleus-centered extracts. As a result, production rates derived from nucleus-centered extracts are underestimated. A multiplicative correction factor known as the growth factor (GF) is applied to the $Q_{\rm nc}$ (e.g., Dello Russo et al. 1998, 2020; DiSanti et al. 2001) to compensate for these effects. Thus, the total production rate, $Q_{\rm tot}$, is given by $Q_{\rm tot} = (Q_{\rm nc})$(GF). The GF is determined through the Q-curve method for analyzing the spatial profiles of emissions (Dello Russo et al. 1998, 2020; Bonev 2005) by averaging signal (summed over multiple lines) from equidistant, diametrically opposite directions along the profile relative to the position of peak emission intensity (DiSanti et al. 2016). We could not calculate a well-constrained GF for some molecules owing to insufficient S/Ns in the wings of the profiles (i.e., along lines of sight increasingly displaced from the position of peak emission intensity). For these molecules (e.g., CH_3OH, H_2CO, NH_3, and C_2H_2), we assumed the GF of either simultaneously measured C_2H_6 (for those obtained within the Lp1 setting) or H_2O (for those obtained with the L-custom setting). For CH_3OH and H_2CO, the assumption of a GF from C_2H_6 is reasonable, given that their spatial profiles, while noisy, are consistent with nucleus-centered sublimation (Figure 2). In addition, seeing-related flux losses are a common systematic effect for all molecular species sampled within a given spectrograph setting. Therefore, they will influence the GF (within a setting) in an identical manner (e.g., Villanueva et al. 2012a; DiSanti et al. 2014; Bonev et al. 2021). Production rates for all the species and their mixing ratios relative to water (and ethane) are presented in Table 2.

4.3. Molecular Mixing Ratios

The compositional taxonomy of comets is based on the measurements of mixing (or abundance) ratios for molecules

Table 2
Volatile Composition of Comet S3 Obtained Using iSHELL

Setting	Molecule	T_{rot} [a] (K)	GF[b]	Q[c] (10^{26} mol s^{-1})	$\frac{Q_X}{Q_{H_2O}}$ [d] (%)	$\frac{Q_X}{Q_{C_2H_6}}$ [e]
2020 Nov 29, $R_h = 0.52$ au, $\Delta = 1.10$ au, $d\Delta/dt = 18.65$ km s^{-1}						
L-custom	H_2O	95 ± 3	3.36 ± 0.32	1490 ± 180	100	266.0 ± 48.34
	HCN	101^{+8}_{-7}	3.43 ± 0.32	3.47 ± 0.41	0.23 ± 0.04	0.62 ± 0.11
		(95)	3.43	3.43 ± 0.41	0.23 ± 0.04	0.61 ± 0.11
	C_2H_2	(95)	(3.36)	2.76 ± 0.42	0.19 ± 0.04	0.49 ± 0.10
	NH_3	(95)	(3.36)	16.3 ± 1.8	1.09 ± 0.19	2.90 ± 0.51
	NH_2	(95)	(3.36)	22.8 ± 2.5	1.53 ± 0.27	4.06 ± 0.71
Lp1	C_2H_6	107^{+17}_{-14}	2.84 ± 0.14	5.90 ± 0.56	0.40 ± 0.06	1
		(95)	2.84	5.61 ± 0.54	0.38 ± 0.06	1.00
	CH_4	(95)	(2.84)	11.2 ± 1.1	0.75 ± 0.12	2.00 ± 0.22
	OH^*	(95)	(2.84)	1140 ± 102	76.5 ± 11.5	203 ± 18
	CH_3OH	106^{+7}_{-6}	(2.84)	24.1 ± 2.2	1.62 ± 0.26	4.29 ± 0.44
		(95)	(2.84)	22.3 ± 2.1	1.50 ± 0.24	3.99 ± 0.41
	H_2CO	106^{+10}_{-9}	(2.84)	5.79 ± 0.63	0.39 ± 0.07	1.03 ± 0.12
		(95)	(2.84)	5.48 ± 0.60	0.37 ± 0.06	0.98 ± 0.12
2020 Dec 1, $R_h = 0.49$ au, $\Delta = 1.12$ au, $d\Delta/dt = 21.67$ km s^{-1}						
M2	H_2O	114 ± 9	3.39 ± 0.38	2210 ± 290	100	267.67 ± 53.56
	CO	121^{+8}_{-7}	3.19 ± 0.32	85.8 ± 9.7	3.89 ± 0.57	10.40 ± 1.89
		(114)	(3.19)	84.4 ± 9.6	3.83 ± 0.56	10.24 ± 1.86
	OCS	(121)	(3.39)	2.25 ± 0.37	0.10 ± 0.02	0.27 ± 0.06
		(114)	(3.39)	2.21 ± 0.37	0.10 ± 0.02	0.27 ± 0.06
L-custom	H_2O	98 ± 4	3.69 ± 0.70	2000 ± 230	100	242.13 ± 59.33
	HCN	86^{+6}_{-5}	(3.69)	4.66 ± 0.94	0.23 ± 0.07	0.57 ± 0.17
		(98)	(3.69)	4.81 ± 0.97	0.24 ± 0.07	0.58 ± 0.17
	C_2H_2	(98)	(3.69)	4.69 ± 1.06	0.24 ± 0.16	0.57 ± 0.18
	NH_3	(98)	(3.69)	16.7 ± 4.4	0.84 ± 0.33	2.02 ± 0.69
	NH_2	(98)	(3.69)	35.7 ± 6.9	1.79 ± 0.54	4.33 ± 1.25
Lp1	C_2H_6	107^{+17}_{-14}	3.14 ± 0.28	8.52 ± 0.86	0.43 ± 0.08	1.00
		(98)	(3.14)	8.23 ± 0.83	0.41 ± 0.07	1.00
	CH_4	(98)	3.19 ± 0.13	14.7 ± 1.90	0.74 ± 0.13	1.79 ± 0.27
	OH^*	(98)	(3.14)	1732 ± 119	86.8 ± 11.8	210 ± 25
	CH_3OH	107 ± 8	(3.14)	32.1 ± 3.10	1.61 ± 0.28	3.89 ± 0.51
		(98)	(3.14)	30.4 ± 3.0	1.53 ± 0.27	3.69 ± 0.60
	H_2CO	85 ± 10	(3.14)	6.73 ± 0.79	0.34 ± 0.06	0.82 ± 0.11
		(98)	(3.14)	7.20 ± 0.84	0.36 ± 0.07	0.87 ± 0.15

Notes.
[a] Rotational temperature. Values in parentheses are assumed.
[b] Growth factor. Values in parentheses are assumed.
[c] Global production rate. Production rate uncertainty includes line-by-line deviation between modeled and observed intensities and photon noise (e.g., Dello Russo et al. 2004; Bonev et al. 2007).
[d] Molecular abundance with respect to H_2O.
[e] Molecular abundance with respect to C_2H_6.

(DiSanti et al. 2021), usually calculated with respect to H_2O (the most abundant molecule in active comets), and is expressed as the ratio of the total production rate of a given molecule to that of H_2O (Q_X/Q_{H_2O}). H_2O is usually observed simultaneously (within the same instrument setting) or contemporaneously (during the same observing block) as the other molecules. The uncertainty in the mixing ratio is calculated considering the uncertainty due to the GF and the stochastic noise or standard error (depending on which one is higher). The uncertainty due to the conversion factor between measured counts (ADU s^{-1}) and flux density (W m^{-2} cm^{-1}), Γ, is also included if the species being considered were observed using a different instrument setting. Since ethane (C_2H_6) is routinely measured in the comae of comets at high S/N, it has recently been used as an alternative compositional baseline molecule for calculating mixing ratios to extend the chemical taxonomy of parent volatiles in comets (e.g., Bonev et al. 2021 and references therein). In the case of S3, C_2H_6 was observed on both dates using the Lp1 setting. The mixing ratios (with respect to H_2O and C_2H_6) of the molecules we targeted during our two nights of observations are given in Table 2.

4.4. Spatial Profiles

Studies of coma molecular emission intensity along the slit (spatial profiles) can provide information on the association of volatiles in the comet nucleus and how they are released into the coma (Dello Russo et al. 2004, 2020). Comparing profiles of co-measured volatiles and dust provides information regarding the release and outflow of material in the coma (e.g., Dello Russo et al. 2004). Such comparisons can also disentangle direct release from the nucleus versus from potential distributed sources in the coma (Dello Russo et al. 1998, 2016a; DiSanti et al. 2001; Brooke et al. 2003). We extracted emission profiles for H_2O, OH^* (OH prompt emission, a proxy for H_2O production rate and spatial profile),

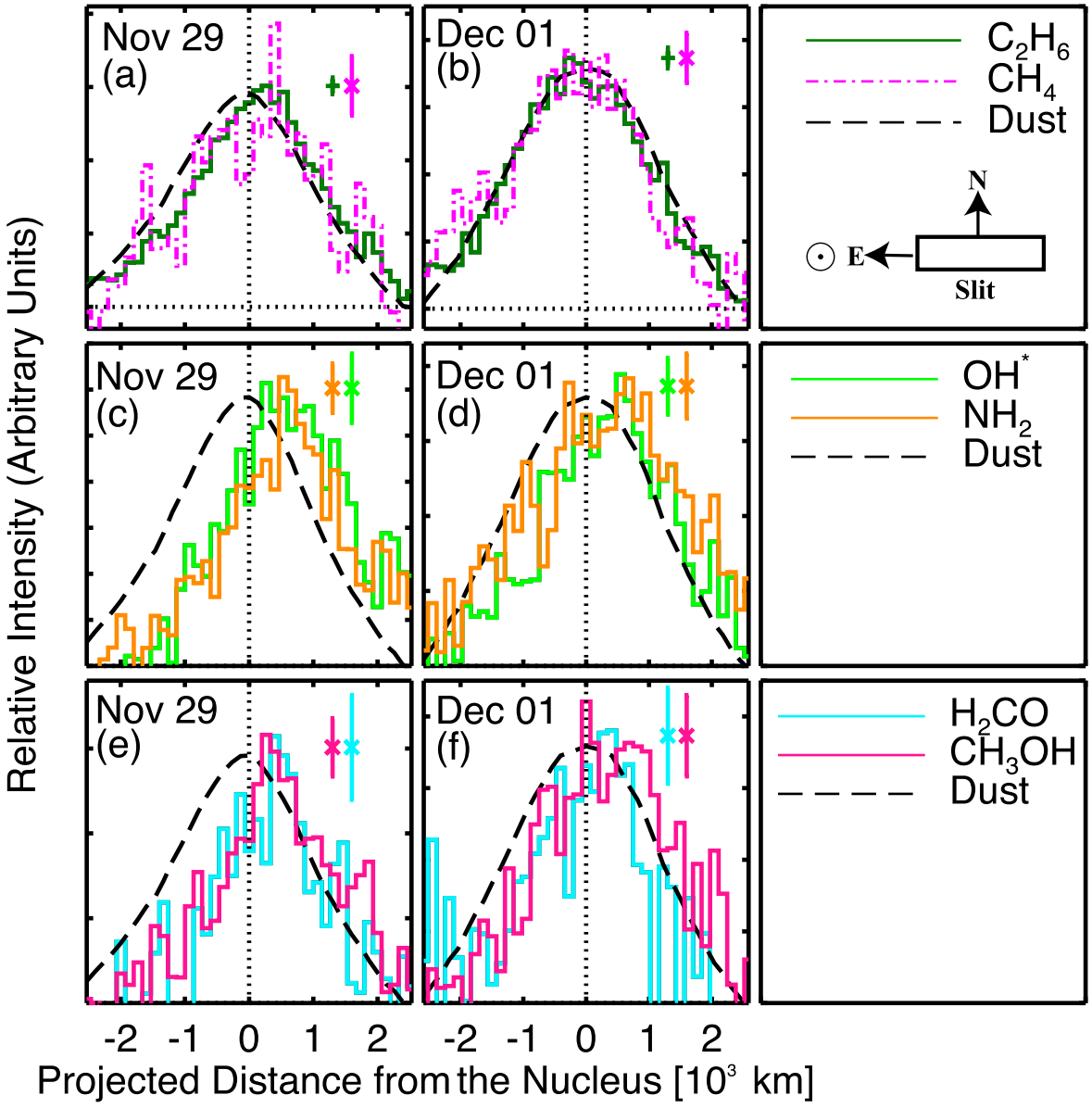

Figure 2. Simultaneously measured spatial profiles on 2020 November 29 (panels (a), (c), and (e)) and December 1 (panels (b), (d), and (f)) using the Lp1 setting. The slit was oriented along the Sun–comet direction of ∼272° and a favorable phase angle of ∼61° on both dates. To ensure uniform spatial registration for all targeted molecular species, the peak of the continuum profile (black dashed line) is taken to define the nucleus position. The vertical error bars indicated for each volatile species represent $\pm 1\sigma$ stochastic noise.

CH_4, NH_2, HCN, CH_3OH, H_2CO, and C_2H_6 in S3 on both dates. We also generated spatial profiles for H_2O, CO, and CN from the M2 setting on UT 2020 December 1 (see Figures 2 and 3).

An important caveat in the interpretation of spatial profiles is that the iSHELL slit is 15″ long. When nodding on chip, the A and B beams are separated by 7.″5 (half the slit length; see Section 2). Therefore, if the comet's emission extends beyond about 3.″75 from the nucleus, taking an A-B will result in the subtraction of some flux in the extended wings of the profiles. The broader the emission spatial profile, the more significant this self-subtraction will be. In addition, some flux may be lost outside the slit for molecules that exhibit a substantial offset relative to the dust continuum since the telescope was tracking on the optocenter during our observations. In the discussion below, most molecules have sufficiently narrow profiles (FWHM < 3″) and small (<0.″5) offsets to not be significantly affected by self-subtraction. The exceptions are species such as CN in the M2 setting and H_2O and OH^* in the L-custom setting (those with high offset toward the antisunward direction and showing highly extended profiles). The variation in OH^*, NH_2, and H_2O profiles among the different dates and settings implies that S3 was exhibiting complex and variable outgassing behavior on relatively short timescales. For this reason, we limit the discussion of the spatial profiles to simultaneously observed molecules for each setting separately.

4.4.1. Lp1

Using the Lp1 setting, we obtained the spatial profiles of C_2H_6, CH_4, CH_3OH, H_2CO, NH_2, and OH^* on both dates (Figure 2). The spatial profiles of the apolar molecules C_2H_6 and CH_4 (Figures 2(a) and (b)) exhibit similar profile shapes and peak positions. While the profile shapes are also very

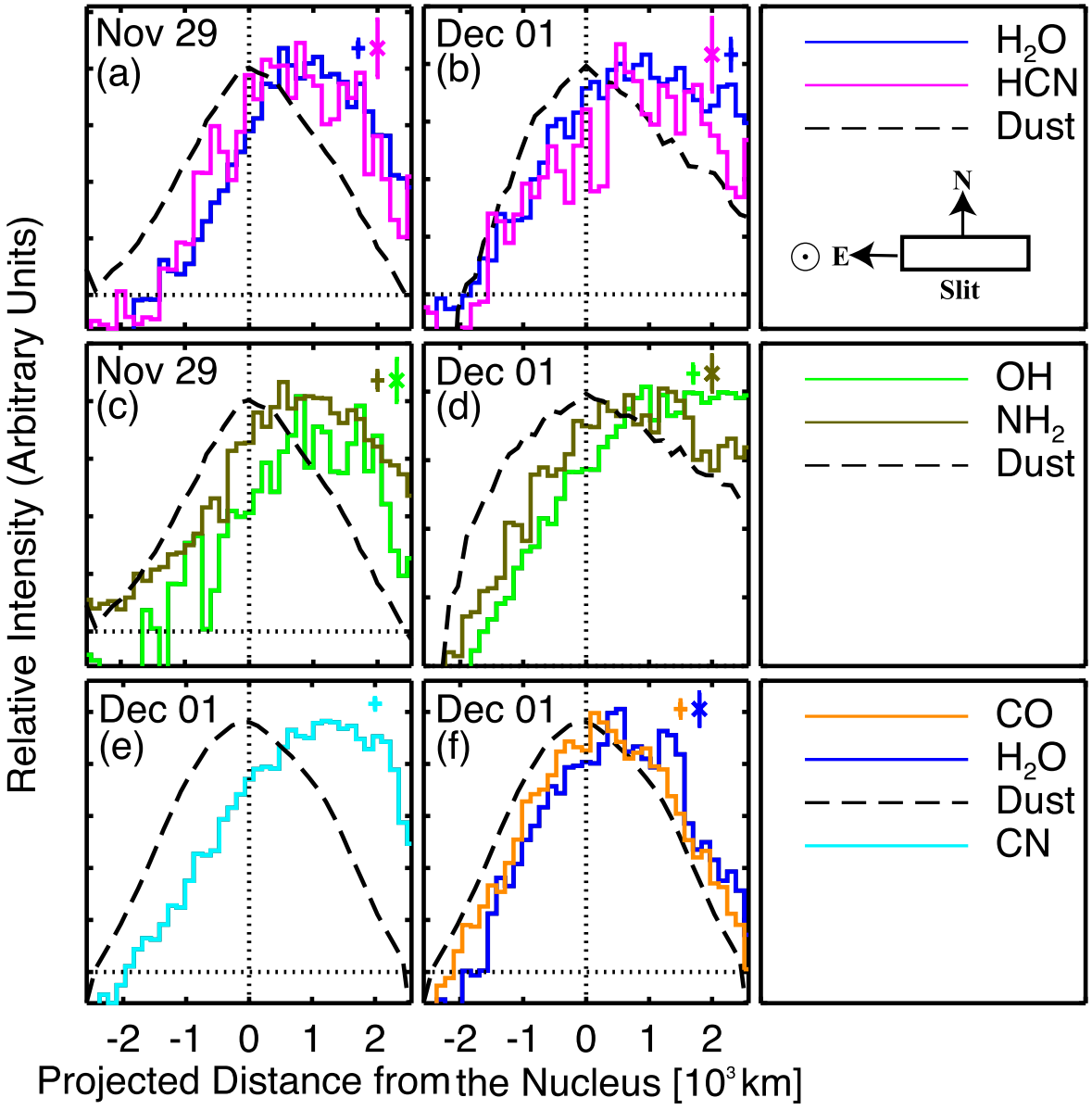

Figure 3. Same as Figure 2 but for H_2O, HCN, OH, and NH_2 measured on 2020 November 29 (panels (a) and (c)) using the L-custom setting and on December 1 using the L-custom setting (panels (b) and (d)) and the M2 setting (panels (e) and (f)).

similar to the co-measured, nearly Gaussian-shaped dust profile, there was a slight shift of the gas profiles toward the antisunward direction on November 29 that was not present on December 1. Symmetric spatial distributions and a similar profile shape to the co-observed dust for these apolar species were noted by Villanueva et al. (2011a) in comet C/2007 W1 (Boattini), by DiSanti et al. (2021, 2014) in comets C/2018 Y1 (Iwamoto) and C/2009 P1 (Garradd), and by Bonev et al. (2017) in comet C/2006 W3 (Christensen), suggesting that these apolar hydrocarbons may have been released primarily from the nucleus.

The spatial profiles of the polar species CH_3OH and H_2CO (Figures 2(e) and (f)), as well as the product species of polar molecules, OH^* and NH_2 (Figures 2(c) and (d)), are consistent with each other on both dates. They are slightly narrower than the profiles of the apolar molecules and shifted more toward the antisunward direction with respect to the co-observed dust profile, with a slightly higher shift on November 29. As discussed in the next section, NH_2 could be produced by fluorescence and prompt emissions, though, as we noted in Section 4.4.2, most of the lines used in the spatial analysis of NH_2 are of lower rotational states for which prompt emission is expected to be insignificant.

4.4.2. L-custom

HCN, OH, and NH_2 were co-measured with H_2O on both dates using the L-custom setting. They all exhibited asymmetry in the antisunward direction, as well as comparable and significant antisunward offsets relative to the dust (see Figures 3(a)–(d)). On December 1, the spatial profiles for all species were broader than on November 29, similar to the pattern seen in the Lp1 spatial profiles (Figures 2 and 3(c) and (d)). We note that OH^* (prompt emission), which tracks the distribution of H_2O, occurs generally at wavenumbers less than $\sim$3410 cm^{-1} (corresponding to higher rotational quantum numbers). Combined OH (fluorescent emission) and OH^*

(prompt emission) is expected for lines at larger wavenumbers (lower rotational excitation). Compared to the OH^* spatial profiles from Lp1, the L-custom OH profile exhibited a greater antisunward offset on both dates and was flatter in the antisunward direction on December 1, extending well beyond the edge of the slit. Such dramatically different outgassing behavior from simultaneously observed water, coupled with the fact that our prompt emission model does not fit the low-J OH emission lines well, could indicate that fluorescence emission contributed significantly in the L-custom setting (Figure 3(d)). This is further supported by noting that the high-J OH lines in Lp1, which are less likely to be excited by fluorescence emission alone, both have similar spatial profiles to other molecules undergoing fluorescent emission and provide a similar water production rate. For this reason, we do not report water production rates inferred from OH lines in the L-custom setting.

NH_2, generally thought to be produced from the photodissociation of NH_3, was also observed for S3. For comets C/2004 Q2 (Machholtz) (Kawakita & Mumma 2011) and 6P/d'Arrest (Dello Russo et al. 2009a), comparison of the mixing ratio of NH_2 and NH_3 supports NH_3 as the dominant parent molecule of NH_2. In the case of S3, assuming the same GF and rotational temperature for both NH_2 and NH_3 results in an NH_2 abundance about twice that of NH_3. Discrepancies in NH_2 and NH_3 abundances have been noted for other comets. For example, Dello Russo et al. (2016b) observed D/2012 S1 (ISON) near $R_h = 0.46$ au and derived a production rate of NH_2 less than that of NH_3 by about a factor of 5, though this could have been due in part to the nonsimultaneous measurement of these molecules and the short-term variability exhibited by comet D/2012 S1, the absence of an appropriate model for a daughter species like NH_2 (Dello Russo et al. 2016b), or the production of NH_2 from a species released when a thermal threshold is reached (Dello Russo et al. 2016a). Even though the R_h at which S3 was observed was similar to that of D/2012 S1, the fact that the production rate of NH_2 was greater than that of NH_3 in S3 as compared to D/2012 S1 (ISON) is intriguing given that the same NH_2 fluorescence model (by Kawakita & Mumma 2011) was used in both comets to obtain the production rates. In this work, in addition to finding the mixing ratio of NH_2, we also analyzed the spatial profiles of NH_2 to characterize the overall outgassing behavior of S3 (see Figure 3). Most of the lines used in the analyses of spatial profiles of NH_2 are of lower rotational quantum states and hence are produced mainly by fluorescence emission. The NH_2 spatial profiles also show similar widths and offsets from the dust to co-measured species HCN and H_2O, which also exhibit fluorescence emission (Figure 3). Due to weak S/N of NH_3 lines, we were not able to obtain the spatial distribution of NH_3 to compare it to that of NH_2 to accurately determine how different the spatial profile of NH_2 is from its likely fluorescent emitted parent molecule NH_3.

4.4.3. M2

Carbon monoxide (CO) and CN were observed simultaneously with H_2O on December 1 using the M2 setting (Figures 3(e) and (f)). CO has a sublimation temperature of ~24 K (Crovisier & Encrenaz 2000), making it the most volatile species observed in comets at IR wavelengths. While the profile shape and width are very similar to those of H_2O, the antisunward shift is slightly smaller (Figure 3(f)). The CN emission spectra, which include very high energy transitions, require a very high temperature (>200 K) and are not well fit by the currently existing fluorescent models (e.g., Dello Russo et al. 2016a, 2016b; Roth et al. 2018). This is consistent with what was observed in the optical for comet D/2012 S1 (ISON) at a similar R_h (A. McKay 2023, private communication), confirming that daughter species have higher rotational excitation temperatures than their parents. Thus, we do not report the production rate or abundance of CN in this work. The spatial profile of CN is highly asymmetric and broad compared to the co-observed dust, with a greater shift toward the antisunward direction than for any other molecule (Figures 2 and 3). Similar behavior was noted for comets D/2012 S1 (Dello Russo et al. 2016b) and 153P/Ikeya-Zhang (Dello Russo et al. 2004), which were observed at similar heliocentric distances. This spatial distribution suggests a different, extended source for CN that does not follow the spatial distribution of the continuum dust. As discussed in Section 5.1, this is further supported by the fact that the HCN production rate in S3 is insufficient to account for the CN observed in the optical (Jehin et al. 2020a, 2020b).

5. Discussion

5.1. Production Rates and Mixing Ratios

H_2O, the most abundant species in the coma of comets, is routinely detected at infrared wavelengths. The H_2O production rate we measured on November 29 using the L-custom setting was $(1.49 \pm 0.18) \times 10^{29}$ molecules s^{-1}, while on December 1, we measured $Q(H_2O)$ of $(2.00 \pm 0.23) \times 10^{29}$ molecules s^{-1} and $(2.22 \pm 0.29) \times 10^{29}$ molecules s^{-1} using L-custom and M2, respectively. Thus, the H_2O production rate on December 1 was higher than its value on November 29, by a factor of ~1.5. This increase in H_2O production rate before perihelion is consistent with the measurements of Combi et al. (2023), who reported a steeply increasing productivity leading up to perihelion.

To obtain the global production rate, our technique to determine the GFs involves averaging along both sides of a spatial profile to average out asymmetries (e.g., Villanueva et al. 2011a). In the scenario where the spatial profiles were sufficiently offset and were considerably off the chip on the right side, we used the left side of the profile to determine the GF. The agreement of H_2O production rates for the L-custom and M2 settings on December 1 demonstrates the robustness of this method. For abundance ratios, co-observed H_2O was used when available, and for species acquired in the Lp1 setting, L-custom H_2O was used since it was observed on both dates. We note that this may lead to systematic differences in abundance, given that the spatial distributions of volatiles in the Lp1 setting are different from that of H_2O in L-custom. However, since the uncertainties in production rates take into account uncertainties in GFs and uncertainty in Γ, the uncertainty introduced into the abundance as a result of using production rates between different settings (nonsimultaneous measurements) is accounted for. We also add that the OH prompt emission in Lp1 gives a H_2O production rate that is consistent with the H_2O production rates in the L-custom setting.

Combi et al. (2023) also reported water production rates from 2020 October 29 through 2021 February 13, using the Solar Wind ANisotropies (SWAN) instrument on board the Solar and Heliospheric Observer (SOHO) satellite. They found a steep R_h^{-5} heliocentric distance dependence as S3 approached perihelion. The increase in the H_2O production rate we observed between the two dates is consistent with this increase;

Table 3
The Volatile Composition of OCCs Measured at $R_h \leqslant 0.80$ au

Comet[a]	R_h (au)	Molecules			
		H_2CO	NH_3	C_2H_2	HCN
S3	0.49–0.52	0.37 ± 0.05	1.09 ± 0.19	0.19 ± 0.04	0.23 ± 0.03
S1	0.35–0.59	1.10 ± 0.30	3.63 ± 0.56	0.24 ± 0.02	0.28 ± 0.02
E4	0.66	0.36 ± 0.03	1.86 ± 0.36	0.14 ± 0.02	0.17 ± 0.02
V5	0.70–0.79	0.13 ± 0.02	0.74 ± 0.08	0.07 ± 0.01	0.08 ± 0.01
153P	0.51–0.78	0.83 ± 0.24	⋯	0.21 ± 0.05	0.21 ± 0.03
T7	0.69	0.79 ± 0.09	⋯	⋯	⋯
P1	0.55	0.49 ± 0.09	1.50 ± 0.30	0.45 ± 0.08	0.24 ± 0.03
F6	0.75	0.54 ± 0.12	⋯	⋯	⋯
B2	0.64–0.73	⋯	⋯	0.25 ± 0.10	0.20 ± 0.03
A1	0.62–0.68	0.14 ± 0.01	<0.34	0.09 ± 0.01	0.11 ± 0.01
	0.62–0.63	0.25 ± 0.02	<0.60	⋯	⋯

Note.
[a] S1 ≡ C/2012 S1 ISON (Dello Russo et al. 2016b; DiSanti et al. 2016), E4 ≡ C/2017 E4 (Faggi et al. 2018), V5 ≡ C/2013 V5 (DiSanti et al. 2018), 153P ≡ 153P/Ikeya-Zhang (DiSanti et al. 2002; Gibb et al. 2003; Dello Russo et al. 2004, 2016a), T7 ≡ C/2002 T7 Linear (DiSanti et al. 2006), P1 ≡ C/2006 P1(Dello Russo et al. 2009b), F6 ≡ C/2012 F6 (Paganini et al. 2014), B2 ≡ C/1996 B2 (Brooke et al. 1996; Dello Russo et al. 2002; Magee-Sauer et al. 2002; DiSanti et al. 2003), A1 ≡ C/2021 A1 (Faggi et al. 2023; Lippi et al. 2023). The abundances indicated for each species are weighted average values when there are multiple measurements for the comet. The uncertainties corresponding to multiple abundance measurements of each species in each comet are either stochastic (weighted uncertainties) or standard error, depending on which value is greater.

however, their absolute production rates are lower than ours by a factor of ∼2–2.5 compared to the same dates. It is not unusual for the SOHO/SWAN water production rates to differ from those measured in the NIR. If the SOHO values are larger, it is often attributed to icy grains releasing water into the coma outside the smaller field of view of instruments like iSHELL. One example was 46P/Wirtanen (Combi et al. 2020; McKay et al. 2021). Similarly, water values reported for comet D/2012 S1 in the NIR (Dello Russo et al. 2016b; DiSanti et al. 2016) were slightly less than those reported by Combi et al. (2014). However, the much larger field of view of SOHO/SWAN ($5^\circ \times 5^\circ$ with $1^\circ \times 1^\circ$ pixels) compared to iSHELL (15″-long slit with $0\farcs16\,\mathrm{pixel}^{-1}$) means that rapid changes in comet productivity will be detected by and leave the field of view of NIR detectors before filling the beam of SOHO/SWAN. Given the difference in outflow velocities, $\sim 1.2\,\mathrm{km\,s^{-1}}$ for primary volatiles in the NIR and $\sim$8–20 $\mathrm{km\,s^{-1}}$ for H atoms produced from photodissociation measured by SOHO (e.g., Combi et al. 2019), a time delay on the order of days would be expected for sensing dramatic production rate changes with SWAN versus iSHELL. Our production rates on November 29 and December 1 are in agreement with those measured by SWAN about 3–5 days later, consistent with this scenario.

Carbonyl sulfide (OCS) is the only sulfur-bearing species with strong fluorescence emission lines at infrared wavelengths and is only measured in ∼10 comets to date, including radio observations (Saki et al. 2020). Thus, our study of S3 provides a vital addition to the abundance measurements of OCS within the comet population. The OCS abundance we measured in S3 is consistent with measurements in other comets (both OCCs and Jupiter-family comets (JFCs)) obtained over R_h ranging from 0.47 to 1.04 au: C/2012 S1 (Dello Russo et al. 2016b), C/2015 ER61 (Saki et al. 2021), 2P/Encke (Roth et al. 2018), and C/2021 A1 (Leonard) (Faggi et al. 2023).

We compared the abundances of secondary species C_2 and CN with respect to simultaneously measured OH from TRAPPIST (Jehin et al. 2020a, 2020b) at $R_h = 0.87$ and 1.42 au to the abundances of HCN and C_2H_2 with respect to co-measured H_2O during both nights of our observations at $R_h = 0.52$ and 0.49 au. The abundances of C_2H_2 and HCN with respect to H_2O are significantly less than those of C_2 and CN, respectively. This possibly indicates additional sources for these daughter molecules. The inconsistency between abundances of daughter species and their potentially primary molecules is also reported by Lippi et al. (2023) in comet C/2021 A1 (Leonard). In general, the inconsistency between abundances of daughter species from cometary ices in the optical and their potential parents in the infrared has been noted in many comets, possibly due to a significant source of C_2 and CN from grains in those comets (Dello Russo et al. 2016a).

5.2. Comparison of S3 Abundance Ratios with Comets Observed at Similar R_h

To better place S3 in context, we compare our measured abundances with other OCCs. It was noted by Dello Russo et al. (2016a) that many comets observed within $R_h \sim 0.8$ au exhibited a systematic enrichment in H_2CO, NH_3, and C_2H_2 relative to comets measured at larger R_h. For example, comet D/2012 S1 (ISON) was observed on several UT dates spanning $R_h = 1.21$–0.35 au and exhibited significant enhancements in abundances of those three molecules, plus HCN, when observed within $R_h \sim 0.6$ au compared with $R_h > 0.8$ au (DiSanti et al. 2016). This suggests an additional source in the coma, possibly from the photodissociation of more complex progenitors associated with dust grains. This gives rise to the question whether NIR spectroscopic measurements of comets near the Sun (within approximately 0.8 au) truly measure only the nucleus composition of these molecules or whether the actual ice abundances are lower than implied by the coma measurements. Since observations of individual comets over a wide range of R_h are generally unavailable, primarily due to observational constraints, we compare the S3 abundances to those obtained for the sample of OCCs measured within ∼0.8 au (see Table 3) and those observed at $R_h > 0.8$ au. Table 4 compares the average abundances of S3 to those of all OCCs observed at R_h greater than 0.8 au from the Sun, all

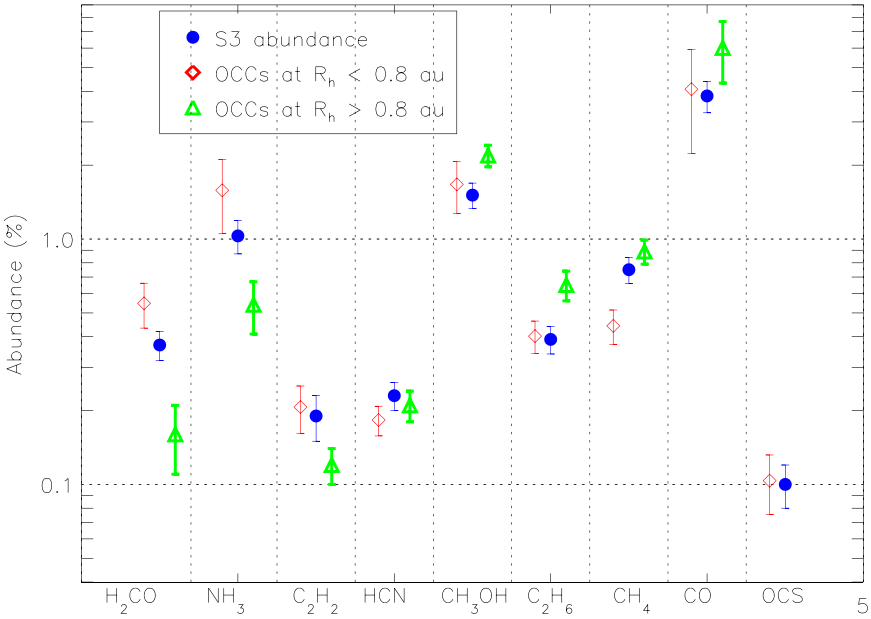

Figure 4. The abundance of primary volatiles in S3 (filled blue circles) compared with weighted average abundance ratios in OCC populations observed in the NIR (at $R_h \leqslant 0.80$ au and $R_h > 0.80$ au).

Table 4
Weighted Mean Abundances for the Detected Molecules in S3

Molecule	Weighted Mean in S3	OCC Average[a] ($R_h > 0.80$ au)	OCC Average[b] ($R_h \leqslant 0.80$ au)	Average in All Comets[d] (%)
C_2H_2	0.19 ± 0.06	0.12 ± 0.02	0.21 ± 0.05	0.12 ± 0.02
HCN	0.23 ± 0.03	0.21 ± 0.03	0.18 ± 0.03	0.20 ± 0.02
NH_3	1.03 ± 0.16	0.54 ± 0.13	1.58 ± 0.53	0.78 ± 0.16
H_2CO	0.37 ± 0.05	0.16 ± 0.05	0.55 ± 0.11	0.27 ± 0.05
CH_3OH	1.51 ± 0.18	2.19 ± 0.22	1.67 ± 0.40	2.20 ± 0.19
C_2H_6	0.39 ± 0.05	0.65 ± 0.09	0.40 ± 0.06	0.53 ± 0.05
CH_4	0.75 ± 0.09	0.89 ± 0.10	0.44 ± 0.07	0.71 ± 0.07
CO	3.83 ± 0.56	6.01 ± 1.69	4.08 ± 1.85	4.15 ± 1.04
OCS	0.10 ± 0.02	⋯	0.10 ± 0.03[c]	0.15 ± 0.04[c]

Notes.
[a] Average abundance values among OCCs measured in NIR at $R_h > 0.8$ au. The uncertainties associated with the unweighted average values correspond to the standard deviation from the mean abundances divided by the square root of the number of measurements.
[b] Average abundance values among OCCs measured in NIR at $R_h \leqslant 0.80$ au, which includes comets listed in Table 3.
[c] Weighted average of OCS from comets observed in the NIR at $R_h \leqslant 0.80$ au: C/2021 A1 (Faggi et al. 2023), C/2012 S1 (Dello Russo et al. 2016b), and C/2002 T7 (Saki et al. 2020).
[d] Average abundance in all comets (OCCs and JFCs) observed in NIR at all R_h values.
[e] C/1995 O1 (Dello Russo et al. 1998), 2P/Encke (Roth et al. 2018), 21P/Giacobini–Zinner (Saki et al. 2020), and OCCs from which the weighted average OCS measurements are indicated in the table.

OCCs observed within 0.8 au from the Sun, and the overall average for all comets. As can be seen from this comparison, when there is a systematic difference in composition for comets observed close to the Sun (as for H_2CO, NH_3, and C_2H_2), the abundance of each molecule in S3 is more similar to the sample of comets observed at small R_h (see Figure 4), consistent with what was found by DiSanti et al. (2016) and Dello Russo et al. (2016b) for comet ISON.

The enhancement in these three volatile species at such a close distance to the Sun might be due to semivolatile sources for these molecular species. For example, ammonium salt species ($NH_4^+Cl^-$, $NH_4^+CN^-$, $NH_4^+OCN^-$, $NH_4^+HCOO^-$, and $NH_4^+CH_3COO^-$) were detected by the Rosetta mission in comet 67P/Churyumov–Gerasimenko (Altwegg et al. 2020). At low temperatures, ammonia easily reacts with acids, such as HCN, HNCO, and HCOOH, to create ammonium salts ($NH_4^+X^-$); thus, they may be present in other cometary nuclei as well (e.g., Altwegg et al. 2020; Poch et al. 2020). Ammonium salts are degraded to ammonia at higher temperatures (at small R_h). Dello Russo et al. (2016b) found a double-peaked NH_3 spatial profile in comet D/2012 ISON, indicative of NH_3 being produced in the coma. The NH_3 lines in S3 were too weak to provide a quality spatial profile, but the strongly enriched NH_3 abundance in S3 possibly hints at ammonium salt as a distributed source in the coma.

The production rate of H_2CO obtained from radio observation for comet C/1995 O1 (Hale–Bopp) also showed an increase with decreasing heliocentric distance (Biver et al. 2002). Apart from additional H_2CO possibly coming from a distributed source (less volatile than H_2CO itself) in a coma, it has been suggested that thermal degradation of formaldehyde polymers, polyoxymethylene (POM), on grains into gaseous H_2CO can explain this increase in production rate (Cottin et al. 2001; Fray et al. 2006). Thus, even though we do not see a clear indication of distributed sources for H_2CO in the spatial distribution for S3, it is possible that the enhancement of H_2CO abundance for S3 at such small R_h could be explained by the same mechanism.

Our results indicate that, compared to the mean abundances among OCCs characterized in the NIR at $R_h > 0.80$ au, S3 is more strongly enriched in H_2CO and NH_3, slightly enriched in C_2H_2, and depleted in CH_3OH and C_2H_6, while it is near average in HCN, CH_4, and CO (see Figure 4). We note that the enrichment in abundances we measured for H_2CO, NH_3, and C_2H_2 is consistent with what DiSanti et al. (2016) and Dello Russo et al. (2016b) found for comet ISON and for the average

of comets measured at $R_h < 0.80$ au. We also compared the abundances measured in S3 to the mean abundances of each species from the overall comet population (JFCs and OCCs together). This comparison indicates that S3 is depleted in CH_3OH and near average in all eight other species measured (see Table 4). We note that even though the relatively large GFs determined for the volatile species of S3 might point to evidence for an extended source, it can also be due to bad seeing for daytime observations of S3, given that the spatial profiles of H_2CO on both dates of our observations do not indicate the presence of a clear extended (distributed) source in the coma (see Figure 2). In general, if the trends in enrichments of some volatile species observed for comets close to the Sun are consistent with the hypothesis that some molecules originate from alternative sources, comets observed beyond 0.8 au might be preferred for overall compositional studies of the nucleus. On the other hand, this implies that comets observed close to the Sun may provide crucial information for explaining processes and molecules that are not generally observable when farther from the Sun.

6. Summary

On UT dates 2020 November 29 and December 1, we obtained pre-perihelion spectra of comet C/2020 S3 (Erasmus) using the echelle spectrograph iSHELL at the NASA IRTF. Our observations spanned a heliocentric distance of $R_h = 0.49$–0.53 au. We report production rates and abundance ratios (relative to simultaneously or contemporaneously measured H_2O) for nine detected trace NIR-active volatiles (C_2H_2, HCN, NH_3, H_2CO, CH_3OH, C_2H_6, CH_4, OCS, and CO). We compared the abundance ratios of molecules measured in S3 to their overall mean abundances in all comets (JFCs and OCCs) measured at NIR wavelengths. Our main conclusions are summarized below.

1. Our results indicate that, compared to the mean abundances in the overall comet population, CH_3OH is depleted; the remaining eight species are consistent with the average comet composition (rightmost column of Table 4). In addition, compared to OCCs measured to date at $R_h > 0.80$ au, S3 is enriched in H_2CO, NH_3, and C_2H_2, which may be due in part to an additional source(s) released in the coma at smaller heliocentric distances (e.g., Dello Russo et al. 2016b, 2016a; DiSanti et al. 2016).
2. Spatial profiles for apolar molecules (CH_4 and C_2H_6) were similar to each other but different from the co-observed polar molecules (H_2CO and CH_3OH or NH_2 and OH^*). Daughter molecules in S3 generally exhibited outgassing behavior with large offsets from the nucleus (Figures 2 and 3). Even though the spatial profiles of most volatile species within the same setting on both dates generally show similar profile shapes and shifts toward the antisunward direction, there are notable differences in the profiles between nonsimultaneous settings, which could be due to temporal variability in outgassing between these nonsimultaneous measurements. Compared to Lp1, the spatial profiles from the L-custom setting show stronger asymmetry in the antisunward direction. Variable outgassing behavior between the settings may be expected as outgassing sources rotate in or out of the field of view (i.e., change in observing geometry).
3. The variable outgassing behavior of comet S3, which is revealed by the spatial profiles measured nonsimultaneously, along with the compositional variations between comets observed at $R_h \leqslant 0.80$ au and $R_h > 0.80$ au, highlights the necessity of observing more comets over a wider range of heliocentric distances, including those that are close to the Sun. The flexible scheduling of IRTF over numerous dates makes these serial measurements a good fit for the iSHELL instrument.

Acknowledgments

Data for this study were obtained with Director's Discretionary Time at the NASA Infrared Telescope Facility (IRTF), operated by the University of Hawai'i under contract NNH14CK55B with NASA. The authors gratefully acknowledge the support of the IRTF staff for their help in acquiring the S3 data. E.G., Y.K., and C.E. acknowledge support from NSF under award AST-2009910. This work was supported by the Planetary Science Division Internal Scientist Funding Program through the Fundamental Laboratory Research (FLaRe) work package (N.X.R.). M.C. gratefully acknowledges the support from NASA SSO Program grant 80NSSC23K0030. B.P.B. acknowledges the NFS award AST-2009398 and NASA award EW 80NSSC20K0341. We also thank the anonymous referee for the helpful comments, which significantly improved the paper.

ORCID iDs

Erika Gibb https://orcid.org/0000-0003-0142-5265
Nathan Roth https://orcid.org/0000-0002-6006-9574
Michael A. DiSanti https://orcid.org/0000-0001-8843-7511
Neil Dello Russo https://orcid.org/0000-0002-8379-7304
Mohammad Saki https://orcid.org/0000-0003-2277-6232
Hideyo Kawakita https://orcid.org/0000-0003-2011-9159
Younas Khan https://orcid.org/0000-0003-4773-2674
Boncho P. Bonev https://orcid.org/0000-0002-6391-4817
Ronald J. Vervack, Jr. https://orcid.org/0000-0002-8227-9564
Michael R. Combi https://orcid.org/0000-0002-9805-0078

References

A'Hearn, M. F., Millis, R. L., Schleicher, D. G., Osip, D. J., & Birch, P. V. 1995, Icar, 118, 223
Altwegg, K., Hans, B., Nora, H., et al. 2020, NatAs, 4, 533
Biver, N., Bockelée-Morvan, D., Colom, P., et al. 2002, EM&P, 90, 5
Biver, N., Bockelée-Morvan, D., Crovisier, J., et al. 2006, A&A, 449, 1255
Bockelée-Morvan, D., Crovisier, J., Mumma, M. J., & Weaver, H. A. 2004, in Comets II, ed. H. A. Weaver, M. C. Festou, & H. U. Keller (Tucson, AZ: Univ. Arizona Press), 391
Bonev, B. P. 2005, PhD thesis, Univ. Toledo
Bonev, B. P., Dello Russo, N., DiSanti, M. A., et al. 2021, PSJ, 2, 45
Bonev, B. P., & Mumma, M. J. 2006, ApJ, 653, 788
Bonev, B. P., Mumma, M. J., Villanueva, G. L., et al. 2007, ApJL, 661, L97
Bonev, B. P., Villanueva, G. L., DiSanti, M. A., et al. 2017, AJ, 153, 241
Brooke, T. Y., Tokunaga, A. T., Weaver, H. A., et al. 1996, Natur, 383, 606
Brooke, T. Y., Weaver, H. A., Chin, G., et al. 2003, Icar, 166, 167
Combi, M. R., Fougere, N., Mäkinen, T. T., et al. 2014, ApJL, 788, L7
Combi, M. R., Mäkinen, T., Bertaux, J.-L., et al. 2020, PSJ, 1, 72
Combi, M. R., Mäkinen, T., Bertaux, J.-L., Quemérais, E., & Ferron, S. 2023, Icar, 398, 115543
Combi, M. R., Mäkinen, T. T., Bertaux, J.-L., Quemérais, E., & Ferron, S. 2019, Icar, 317, 610

Cottin, H., Gazeau, M. C., Benilan, Y., & Raulin, F. 2001, ApJ, 556, 417
Crovisier, J., Bockelee-Morvan, D., Colom, P., et al. 2004, A&A, 418, 1141
Crovisier, J., & Encrenaz, T. 2000, in Comet Science, ed. S. Lyle & R. M. Bonnet (Cambridge: Cambridge Univ. Press), 187
Dello Russo, N., DiSanti, M. A., Magee-Sauer, K., et al. 2004, Icar, 168, 186
Dello Russo, N., DiSanti, M. A., Mumma, M. J., Magee-Sauer, K., & Retting, T. W. 1998, Icar, 135, 377
Dello Russo, N., Kawakita, H., Bonev, B. P., et al. 2020, Icar, 335, 113411
Dello Russo, N., Kawakita, H., Vervack, R. J., Jr., & Weaver, H. A. 2016a, Icar, 278, 301
Dello Russo, N., Mumma, M. J., DiSanti, M. A., & Magee-Sauer, K. 2002, JGR, 107, 5095
Dello Russo, N., Vervack, R. J., Weaver, H. A., et al. 2009a, ApJ, 703, 187
Dello Russo, N., Vervack, R. J., Jr., Kawakita, H., et al. 2016b, Icar, 266, 152
Dello Russo, N., Vervack, R. J., Jr., Weaver, H. A., & Lisse, C. M. 2009b, Icar, 200, 271
DiSanti, M. A., Bonev, B. P., Dello Russo, N., et al. 2017, AJ, 154, 246
DiSanti, M. A., Bonev, B. P., Dello Russo, N., et al. 2021, PSJ, 2, 225
DiSanti, M. A., Bonev, B. P., Gibb, E. L., et al. 2016, ApJ, 820, 34
DiSanti, M. A., Bonev, B. P., Magee-Sauer, K., et al. 2006, ApJ, 650, 470
DiSanti, M. A., Bonev, B. P., Villanueva, G. L., & Mumma, M. J. 2013, ApJ, 763, 1
DiSanti, M. A., Dello Russo, N., & Magee-Sauer, K. 2002, ACM 2002, 500, 571
DiSanti, M. A., Mumma, M. J., Dello Russo, N., Magee-Sauer, K., & Griep, D. M. 2003, JGR, 108, 5061
DiSanti, M. A., Mumma, M. J., Dello Russo, N., & Magee-Sauer, K. 2001, Icar, 153, 361
DiSanti, M. A., Villanueva, G. L., Paganini, L., et al. 2014, Icar, 228, 167
DiSanti, Michael A., Bonev, B. P., Gibb, E. L., et al. 2018, AJ, 156, 258
Eistrup, C., Walsh, C., & van Dishoeck, E. F. 2019, A&A, 629, A84
Faggi, S., Lippi, M., Mumma, M. J., & Villanueva, G. L. 2023, PSJ, 4, 8
Faggi, S., Villanueva, G. L., Mumma, M. J., & Paganini, L. 2018, AJ, 156, 68
Fray, N., Benilan, Y., Biver, N., et al. 2006, Icar, 184, 239
Gibb, E. L., Mumma, M. J., Dello Russo, N., DiSanti, M. A., & Magee-Sauer, K. 2003, Icar, 165, 391
Huebner, W. F., & Mukherjee, J. 2015, P&SS, 106, 11
Jehin, E., Moulane, Y., Manfroid, J., Pozuelos, F., & Hutsemekers, D. 2020a, ATel, 14101, 1
Jehin, E., Moulane, Y., Manfroid, J., et al. 2020b, ATel, 14174, 1
Kawakita, H., & Mumma, M. J. 2011, ApJ, 727, 91
Królikowska, M., & Dybczynski, P. A. 2017, MNRAS, 472, 4634
Lippi, M., Vander Donckt, M., Faggi, S., et al. 2023, A&A, 676, A105
Magee-Sauer, K., Mumma, M. J., DiSanti, M. A., & Dello Russo, N. 2002, JGR, 107, 5096
McKay, A. J., DiSanti, M. A., Cochran, A. L., et al. 2021, PSJ, 2, 21
Mumma, M. J., & Charnley, S. B. 2011, ARA&A, 49, 471
Nakano Note 4506, (Nakano wa Kangaeru noda), NK, https://www.oaa.gr.jp/~oaacs/nk/nk4506.htm
Paganini, L., DiSanti, M. A., Mumma, M. J., et al. 2014, AJ, 147, 15
Poch, O., Istiqomah, I., Quirico, E., et al. 2020, Sci, 367, 1212
Radeva, Y. L., Mumma, M. J., Bonev, B. P., et al. 2010, Icar, 206, 764
Rayner, J., Tokunaga, A., Jaffe, D., et al. 2022, PASP, 134, 015002
Roth, N. X., Gibb, E. L., Bonev, B. P., et al. 2018, AJ, 156, 251
Saki, M., Gibb, E. L., Bonev, B. P., et al. 2020, AJ, 160, 184
Saki, M., Gibb, E. L., Bonev, B. P., et al. 2021, AJ, 162, 145
Villanueva, G. L., Disanti, M. A., Mumma, M. J., & Xu, L.-H. 2012a, ApJ, 747, 37
Villanueva, G. L., Smith, M. D., Protopapa, S., Faggi, S., & Mandell, A. M. 2018, JQSRT, 217, 86
Villanueva, G. L., Magee-Sauer, K., & Mumma, M. J. 2013, JQSRT, 129, 158
Villanueva, G. L., Mumma, M. J., Bonev, B. P., et al. 2012b, JQSRT, 113, 202
Villanueva, G. L., Mumma, M. J., DiSanti, M. A., et al. 2011a, Icar, 2016, 227
Villanueva, G. L., Mumma, M. J., & Magee-Sauer, K. 2011b, JGR, 116, E08012
Vokrouhlicky, D., Nesvorny, D., & Dones, L. 2019, AJ, 157, 181
Willacy, K., Turner, N., Bonev, B., et al. 2022, ApJ, 931, 164